

# Dalton Transactions

An international journal of inorganic chemistry

Accepted Manuscript

This article can be cited before page numbers have been issued, to do this please use: P. Halaš, I. Nemeč, E. Cizmar and R. Herchel, *Dalton Trans.*, 2025, DOI: 10.1039/D5DT01004G.



This is an Accepted Manuscript, which has been through the Royal Society of Chemistry peer review process and has been accepted for publication.

Accepted Manuscripts are published online shortly after acceptance, before technical editing, formatting and proof reading. Using this free service, authors can make their results available to the community, in citable form, before we publish the edited article. We will replace this Accepted Manuscript with the edited and formatted Advance Article as soon as it is available.

You can find more information about Accepted Manuscripts in the [Information for Authors](#).

Please note that technical editing may introduce minor changes to the text and/or graphics, which may alter content. The journal's standard [Terms & Conditions](#) and the [Ethical guidelines](#) still apply. In no event shall the Royal Society of Chemistry be held responsible for any errors or omissions in this Accepted Manuscript or any consequences arising from the use of any information it contains.

## ARTICLE

Elucidation of *trans/cis*-isomerization of cinnamate ligand on structural, spectroscopic and magnetic properties of cobalt(II) single-molecule magnetsPetr Halaš,<sup>a</sup> Ivan Nemeč,<sup>a</sup> Erik Čížmár<sup>b</sup> and Radovan Herchel<sup>\*a</sup>Received 00th January 20xx,  
Accepted 00th January 20xx

DOI: 10.1039/x0xx00000x

Two new pseudo-octahedral Co(II) complexes **1** [Co(neo)<sub>2</sub>(*trans*-cin)]ClO<sub>4</sub> and **2** [Co(neo)<sub>2</sub>(*cis*-cin)]ClO<sub>4</sub> with *trans* and *cis*-cinnamic acid (Hcin) and neocuproine (neo) as ligands were prepared. Both complexes were characterized via single-crystal X-ray analysis, infrared spectroscopy, magnetic measurements, and EPR spectroscopy. DC magnetic susceptibility measurements revealed large axial magnetic anisotropy with axial zero-field splitting (ZFS) parameters  $D = 49.9$  and  $59.5 \text{ cm}^{-1}$ , and rhombicity  $E/D = 0.307$  and  $0.147$  for **1** and **2**, respectively. These results were in accordance with CASSCF/NEVPT2 calculations. AC magnetic data showed the presence of slow relaxation of magnetization for both compounds in the applied DC field. UV irradiation studies in solution show that complexes most likely undergo *trans/cis* photoisomerisation, which is, however, accompanied by side reactions and degradation. This was elucidated further utilizing DFT and TD-DFT calculations.

## Introduction

Mononuclear single-molecule magnets (SMMs) represent a group of compounds exhibiting slow relaxation of magnetization on the level of single molecules, where only one metallic center is responsible for such behavior. In the past twenty years, progress has been made in improving the blocking temperature, with more recent dysprosocenium derivative [(Cp<sup>iPr5</sup>)Dy(Cp\*)][B(C<sub>6</sub>F<sub>5</sub>)<sub>4</sub>] complex (Cp<sup>iPr5</sup> = penta(isopropyl)cyclopentadienyl, Cp\* = pentamethylcyclopentadienyl) reaching  $T_B = 80 \text{ K}$ , thus surpassing liquid nitrogen temperature.<sup>1</sup>

One of the main drawbacks of the dysprosocenium complexes is their low stability in the air, which has led many researchers to investigate transition metal complexes, mostly limited to Fe(II) and Co(II), to find more stable and easier to synthesize alternatives, albeit exhibiting lower blocking temperatures and barriers compared to Ln(III) SIMs. Polyhedron shapes such as trigonal prism<sup>2</sup> and deformed tetrahedron<sup>3</sup> seem to be the most promising to obtain highly negative  $D$ -parameter with low rhombicity, and thus axial type of magnetic anisotropy and low probability of quantum tunnelling effect in Co(II) complexes. A prominent result was reported by Rechkemmer et al. for (HNEt<sub>3</sub>)<sub>2</sub>[Co(bmsab)<sub>2</sub>] complex (bmsab = N,N'-1,2-phenylenebis(methanesulfonamide))<sup>4</sup>. This Co(II) based SIM possesses axially elongated tetrahedral geometry

and exhibits  $U_{\text{eff}}$  of over  $200 \text{ cm}^{-1}$  together with slow relaxation of magnetization in zero applied static field while also being completely air- and moisture-stable.

Previous research has also shown that an axial type of anisotropy could be observed for octahedral Co(II) complexes with positive  $D$ -parameter and high rhombicity, leading to slow relaxation of magnetization under the applied field.<sup>5</sup> It was concluded that increasing rhombicity causes the transition of the equatorial type of anisotropy into axial for positive  $D$  values. Another approach to synthesizing octahedral Co(II) SIMs was also published by Vallejo et al., utilizing neocuproine and benzoic acid as ligands, which yield deformed octahedral geometry possessing high anisotropy of the axial type.<sup>6</sup> Complexes of 3d metals are, therefore, still of much interest as they can provide much better stability and more facile synthetic procedures without the need for inert or anhydrous conditions.

For SMMs, spin state switching of the bulk samples is usually affected by the magnetic field, however, technological limitations arise when one tries to focus the magnetic field onto a scale of single molecules. Focus has, therefore, been given to pathways that affect spin state switching other than with the magnetic field, such as light irradiation. In the past, many complexes containing azo-<sup>7</sup> or olefin<sup>8</sup> moieties, well known for their photoisomerization, have been prepared,<sup>9</sup> however only limited research has been done on the influence of light-switchability on molecular magnetism.<sup>10,11</sup> Photoisomerisation of azo-compounds or olefins is usually limited to liquid phase as crystal packing hinders the switching action, however, this obstacle may be overcome when working with single-molecule layers or polymeric films.<sup>12</sup> Additionally, problems with the reversibility of photoisomerisable compounds may arise due to degradation or side reactions taking place, such as [2+2] cycloaddition.<sup>13</sup>

<sup>a</sup> Department of Inorganic Chemistry, Faculty of Science, Palacký University, 17. listopadu 12, 771 46 Olomouc, Czech Republic

<sup>b</sup> Institute of Physics, Faculty of Science, P.J. Šafárik University, Park Angelinum 9, 04154 Košice, Slovakia

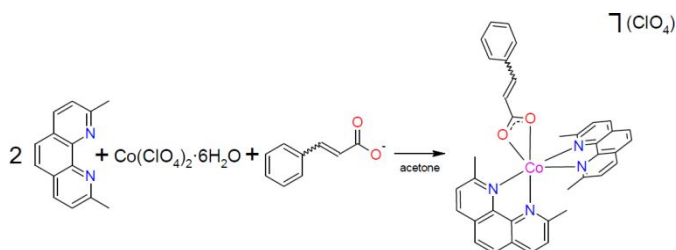
\* Footnotes relating to the title and/or authors should appear here.

Supplementary Information available: [details of any supplementary information available should be included here]. See DOI: 10.1039/x0xx00000x



We have previously reported on the synthesis and magnetochemical characterization of a new Co(II) complex containing neocuproine and *trans*-cinnamic acid as ligands and [BPh<sub>4</sub>]<sup>-</sup> as counterion, exhibiting slow relaxation of magnetization, however, no photoisomerisation could be observed in the solid phase.<sup>14</sup> As *cis* isomer of cinnamic acid can be easily prepared by known methods utilizing UV irradiation,<sup>15,16</sup> we decided to explore and synthesize complexes with both isomers to compare their magnetochemical properties in order to evaluate their potential for future usage as light-switchable SIM-containing materials. Additionally, we chose to utilize a smaller perchlorate anion instead of tetraphenylborate to avoid difficulties with resolving solvent molecules trapped in cavities in the crystal structure.

We herein report on the synthesis and physicochemical characterization of two new Co(II) complexes **1** [Co(neo)<sub>2</sub>(*trans*-cin)]ClO<sub>4</sub> and **2** [Co(neo)<sub>2</sub>(*cis*-cin)]ClO<sub>4</sub> with *trans* and *cis*-cinnamic acid and neocuproine as ligands, together with comparison of their magnetic properties studied by DC and AC magnetic susceptibility measurements, as well as EPR spectroscopy. The aim of this work is to study the effects that *cis-trans* isomerism can have on both static and dynamic magnetic properties, such as zero-field splitting parameters or spin relaxation mechanisms.



Scheme 1 – Synthesis of compounds **1** and **2**.

## Results and discussion

### Synthesis

N-butylammonium salt of *cis*-cinnamic acid was prepared according to a procedure published by Salum et al. utilizing the medium-pressure mercury lamp, providing the ligand in low to moderate yields.<sup>16</sup> The coupling constant obtained by <sup>1</sup>H NMR, together with a comparison of spectra with published ones, confirmed that *cis* isomer has indeed been prepared (Figure S1).

Complexes were synthesized in a simple fashion by first mixing cobalt(II) perchlorate and neocuproine in a 1:2 ratio in acetone and subsequently adding acetone solution of 1 equivalent of the corresponding cinnamate salt. Complex **1** formed big crystals over several days of slow evaporation, while complex **2** precipitated out of solution almost immediately and single crystals suitable for X-ray diffraction had to be grown in extremely dilute solution (scale of 0.01 mmol in several ml of solvent). Products were then collected by filtration, washed with acetone, and dried in air. Polycrystalline products were then characterized by infrared spectroscopy (Figures S2 and S3) and elemental analysis.

To confirm phase purity, we performed X-ray powder diffraction (Figure S4 and S5). Compound **1** did not contain any noticeable impurities. However, compound **2** consistently contains small amounts of unknown impurities or phases even after repeated resyntheses. The elemental analysis confirmed sufficient purity of **2**, and we observed no impurities in magnetochemical studies.

### Crystal structures

Both complexes crystallize in the *P*2<sub>1</sub>/*n* space group and possess 4 molecules per unit cell with Co(II) centres being hexacoordinate with {N<sub>4</sub>O<sub>2</sub>} chromophore (Figure 1). Similarly to our previously published results,<sup>14</sup> octahedral geometry is deformed due to steric hindrance provided by methyl groups of neocuproine and small bite angle of donor oxygen atoms of cinnamate. Within crystal packing,  $\pi$ - $\pi$  stacking interactions between the neocuproine rings are the only notable non-covalent contacts.

Cinnamate ligand is disordered in complex **1** with  $d(\text{Co1-O1}) = 2.077(4)$  Å,  $d(\text{Co1-O2}) = 2.319(4)$  Å and  $\angle(\text{O1-Co1-O2}) = 58.9(2)^\circ$  for fragment with occupancy of 0.678, and  $d(\text{Co1-O1}) = 2.069(9)$  Å,  $d(\text{Co1-O2}) = 2.313(1)$  Å and  $\angle(\text{O1-Co1-O2}) = 58.1(4)^\circ$  for fragment with occupancy of 0.322. Analysis with Shape 2.1 software confirmed that the polyhedron shape is indeed closest to the octahedral one, with continuous shape measure (CShM) values of 3.684 and 4.020 for the disordered fragments, respectively. A small cavity can be found using a 1.2 Å probe radius within the structure, occupying 0.3% of the unit cell volume.

In complex **2**, oxygen atoms are coordinated at nearly equal distances, with  $d(\text{Co1-O1}) = 2.182(1)$  Å,  $d(\text{Co1-O2}) = 2.153(1)$  Å and  $\angle(\text{O1-Co1-O2}) = 60.92(5)^\circ$ . Similarly to complex **1**, the shape of the polyhedron is a deformed octahedron with a CShM value of 2.968. Again, small voids can be found within the structure, occupying 2.5% of unit cell volume. Bond lengths and angles of the coordination polyhedra are summarized in Table S1.

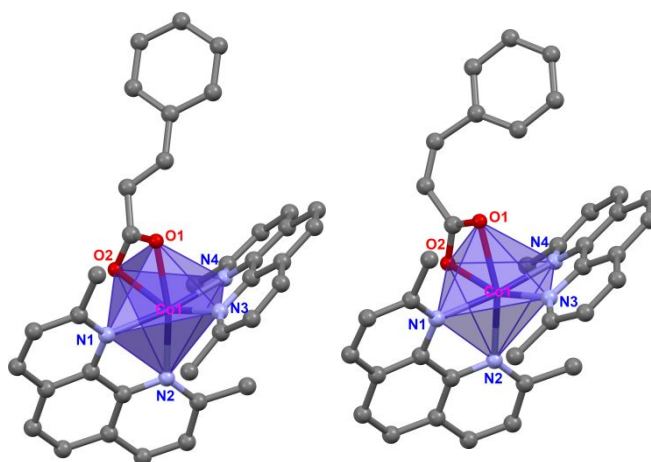


Figure 1 – Structure of complex cations of **1** (left) and **2** (right) with coordination sphere labeled. Hydrogen atoms were omitted for clarity.



### Static magnetic properties

Temperature dependence of magnetic moment at inset field of  $B = 0.2$  T and field dependence of molar magnetization for both complexes at temperatures of  $T = 1.8, 5, 10,$  and  $15$  K are presented in Figure 2. Measured effective magnetic moments at room temperature of  $\mu_{\text{eff}}/\mu_B = 4.69$  for complex **1** and  $\mu_{\text{eff}}/\mu_B = 4.66$  for complex **2** are much higher than the calculated spin-only value of  $\mu_{\text{eff}}/\mu_B = g\sqrt{S(S+1)} = 3.87$  for Co(II) system with  $S = 3/2$  and  $g = 2.0$ , most likely due to large unquenched orbital momentum. As shown in Figure 2,  $\mu_{\text{eff}}/\mu_B$  gradually decreases with lowering temperature down to 3.65 and 3.45 for **1** and **2**, respectively. Furthermore, isothermal molar magnetization at 1.8 K and 7 T reached  $M_{\text{mol}}/(N_A\mu_B) = 2.14$  and 2.06 for **1** and **2**, respectively, values much lower than the calculated  $M_{\text{mol}}/(N_A\mu_B) = g \cdot S = 3$ .

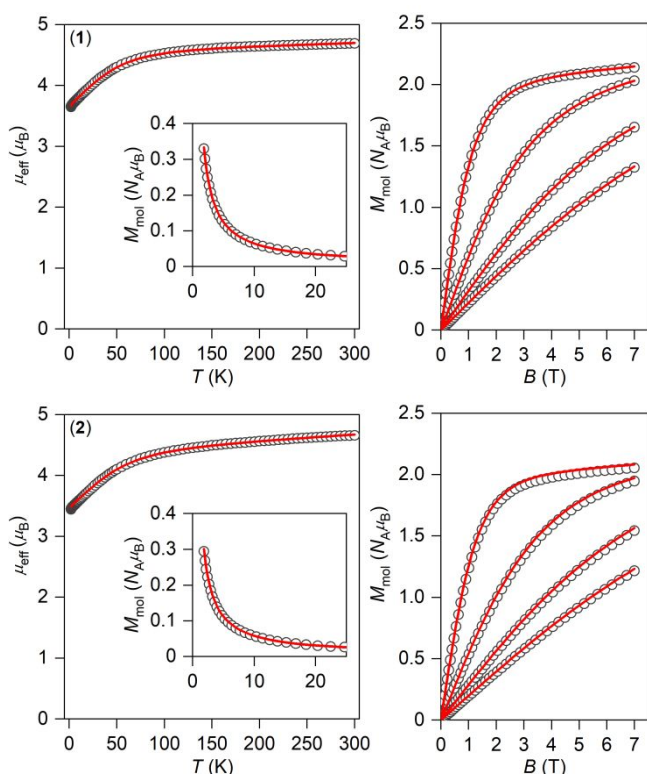


Figure 2 – Temperature dependence of magnetic moment and isothermal field dependence of molar magnetization of **1** (top) and **2** (bottom). Empty symbols – experimental data, full red lines – calculated data.

This suggests that both complexes have large magnetic anisotropy and we therefore performed simultaneous fit of the aforementioned data with spin Hamiltonian (Equation 1) comprising zero-field terms and Zeeman term using POLYMAGNET software.<sup>17</sup>

$$\hat{H} = D(\hat{S}_z^2 - \hat{S}^2/3) + E(\hat{S}_x^2 - \hat{S}_y^2) + \mu_B B g \hat{S} \quad (1)$$

Parameters  $D$  and  $E$  represent axial and rhombic zero-field splitting parameters, respectively. The best fit for complex **1** was obtained with parameters  $D = 49.9$   $\text{cm}^{-1}$ ,  $E/D = 0.307$ ,  $g_{xy} =$

2.470 with  $g_z$  fixed at 2.0 and temperature-independent paramagnetism of  $\chi_{\text{TIP}} = 8.0 \times 10^{-9}$   $\text{m}^3 \text{mol}^{-1}$ . DOI: 10.1039/D5DT01004G

For complex **2**, the best fit was achieved with parameters  $D = 59.5$   $\text{cm}^{-1}$ ,  $E/D = 0.147$ ,  $g_{xy} = 2.347$  with  $g_z$  fixed at 2.0 and temperature-independent paramagnetism of  $\chi_{\text{TIP}} = 15.1 \times 10^{-9}$   $\text{m}^3 \text{mol}^{-1}$ . It should be noted that analogous analysis was attempted with negative  $D$ -values and zero and non-zero rhombicity for both complexes, but without reaching better agreement with the experimental data.

### Dynamic magnetic properties

To investigate the presence of slow relaxation of magnetization, AC susceptibility measurements were performed for both complexes. First, AC susceptibility was measured at a fixed temperature of 2 K with varying static magnetic field. Data were fitted utilizing SciPy module for Python.<sup>18</sup>

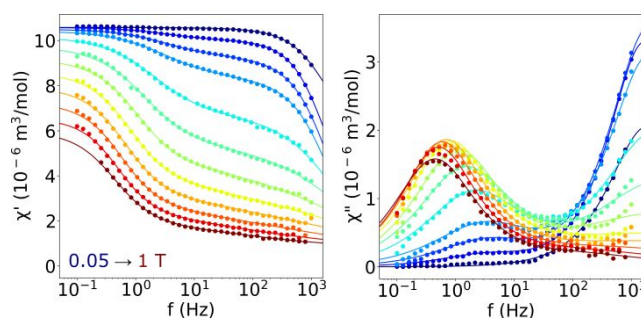
Field-dependence of AC susceptibility could be analyzed in the field range of 0.05 to 1 T for complex **1** (Figure 3). No out-of-phase susceptibility was observed at zero DC field. We observed the appearance of high frequency relaxation channel at lower fields and additional low frequency relaxation channel at higher fields. Experimental data was fitted into one-component or two-component Debye model for fields above 0.05 T, according to Equation 2.

$$\chi(2\pi f) = \chi_S + \sum_{n=1} \frac{\chi_{Tn} - \chi_{Tn-1}}{1 + (i2\pi f \tau_n)^{1-\alpha_n}} \quad (2)$$

Fitted parameters are summarized in ESI (Table S3). Attempts were made to fit the obtained relaxation times simultaneously with temperature-dependent ones, however, no decent fit was obtained, therefore both datasets were analyzed separately. Low frequency channel relaxation times were fitted using the following Equation 3, composed of quantum tunneling (QTM) ( $b_1$ ,  $b_2$ ) and phonon bottleneck (PB) ( $G$ ) terms.

$$\frac{1}{\tau} = \frac{b_1}{1 + b_2 B^2} + G T^2 \quad (3)$$

Best fitted parameters were  $b_1 = 26.2(2.3)$   $\text{s}^{-1}$ ,  $b_2 = 15.0(1.9)$   $\text{T}^{-2}$  and  $G = 0.22(0.01)$   $\text{K}^{-2} \text{s}^{-1}$ . It should be noted that a similar but slightly worse fit was obtained with QTM and direct terms. This is in accordance with the used QTM+PB model as PB is just a hindered direct process.<sup>19</sup> High-frequency relaxation channel was not analyzed further due to large uncertainty, especially at high fields, of the obtained relaxation times.



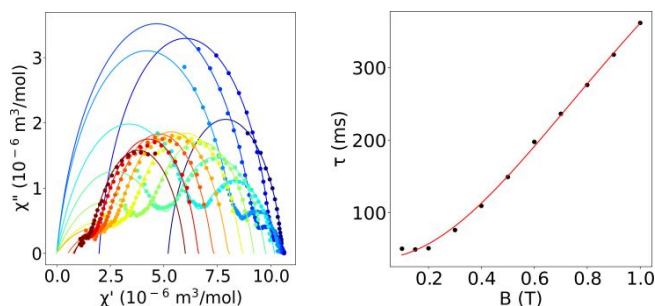


Figure 3 – Field-dependent AC susceptibility data of **1**. Top – real (left) and imaginary (right) parts of susceptibility vs. frequency. Lines represent the best fit into Debye model. Bottom – Argand diagram (left) and best fit of relaxation times (right).

Next, temperature dependence of AC magnetic susceptibility was analyzed in the range of 1.9 to 2.8 K. At higher temperatures, the out-of-phase susceptibility diminished too much to provide any reliable fits. The static field was set to 0.5 T. Data was measured up to 997 Hz, however this was not enough to properly describe the high-frequency relaxation channel, which again resulted in deviations of relaxation times being higher than fitted values. We, therefore, decided to fit only the low-frequency relaxation channel up to 18 Hz into the one-component Debye model (Figure 4, Table S4). Obtained relaxation times were fitted into Equation 4 comprises Raman (C) term. It should be noted that attempts were made to fit data into models containing Orbach term, however obtained values of barrier energy were not in accordance with DC magnetic measurements (Figure S6).

$$\frac{1}{\tau} = CT^n \quad (4)$$

Obtained parameters were  $C = 1.19(0.08) \text{ s}^{-1}\text{K}^{-n}$  and  $n = 2.56(0.09)$ . As the coefficient  $n$  is much closer in value to 2 rather than to the expected range of 5 to 9 for Kramers doublets, we suspect that it is indeed the aforementioned phonon bottleneck process.

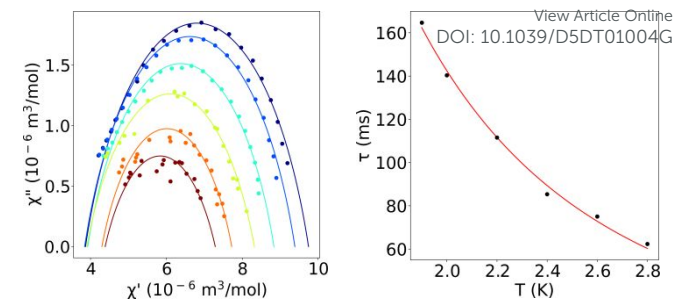
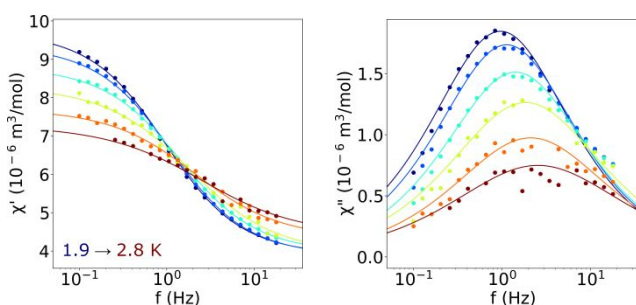


Figure 4 – Temperature-dependent AC susceptibility data of **1**. Top – real (left) and imaginary (right) parts of susceptibility vs. frequency. Lines represent the best fit into the Debye model. Bottom – Argand diagram (left) and best fit of relaxation times (right).

Similarly, for complex **2**, increasing the magnetic field also leads to the increase in out-of-phase AC susceptibility and the consequent appearance of a second relaxation process at higher fields, as can be seen in Figure 5. Thus, data were fitted into one-component, and for fields above 0.15 T, into two-component, Debye model according to Equation 2. Maximal out-of-phase susceptibility was obtained at 0.15 T. Therefore, subsequent temperature-dependent data were measured at a fixed DC field of 0.15 T in the range of 1.9 to 5 K and fitted into a one-component Debye model. Fitted parameters are reported in ESI – Tables S5 and S6. The low-frequency channel was analyzed separately and fitted into a model comprised of QTM (Figure S7). Obtained relaxation times from field- and temperature-dependent data of the high-frequency process were then fitted simultaneously with Equation 5, containing direct (A) and Raman (C,  $n$ ) relaxation process terms (Figure 5). Exponent value  $m$  was set to 4, as Co(II) is a Kramers ion.

$$\frac{1}{\tau} = CT^n + ATB^m \quad (5)$$

This yielded parameters  $C = 173(9) \text{ s}^{-1}\text{K}^{-n}$ ,  $n = 2.15(0.07)$  and  $A = 14552(1107) \text{ s}^{-1}\text{K}^{-1}\text{T}^{-4}$ . As  $n$  is again much lower than the expected values of 5 to 9, we suspect that the Raman relaxation mechanism is rather a phonon bottleneck effect. Attempts were again made to fit the data into models containing Orbach term, however, obtained barrier values were not in accordance with DC magnetic measurements (Figure S8).

Field-dependent data

Temperature-dependent data



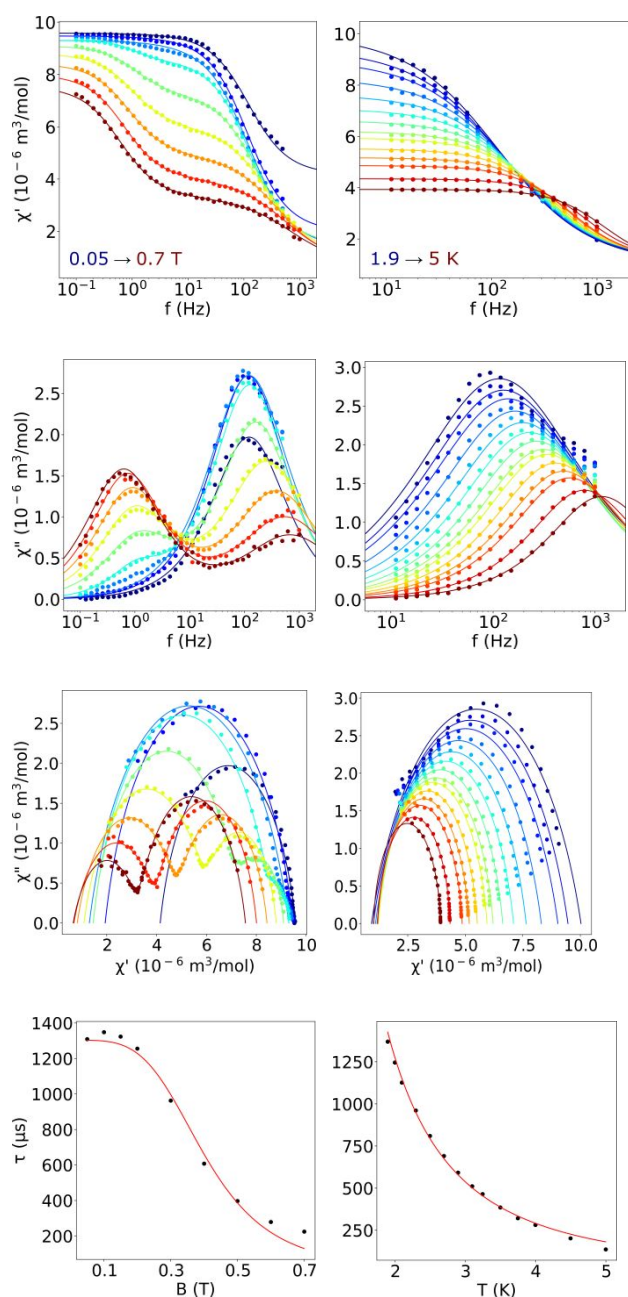


Figure 5 – Field-dependent (left) and temperature-dependent (right) AC susceptibility of **2**. Real (1<sup>st</sup> row) and imaginary (2<sup>nd</sup> row) parts of susceptibility vs. frequency. Lines represent the best fit into the Debye model. Argand diagrams (3<sup>rd</sup> row) and best simultaneous fit of relaxation times (4<sup>th</sup> row).

### EPR spectroscopy

The X-band EPR spectra of compounds **1** and **2** were measured in the temperature range from 2 K to 70 K. A typical decrease of the signal intensity and line broadening with increasing temperature was observed as expected for a large zero-field splitting between the lowest Kramers doublets (Figure S9). Thus, a simplified effective spin  $S_{\text{eff}} = 1/2$  model describing only the ground Kramers doublet for the analysis of EPR at low temperatures can be applied. The mixing of higher excited states with the ground Kramers doublet as a

consequence of the spin-orbit coupling then yields highly anisotropic effective  $g$ -factors. The simulation of EPR spectra shown in Figure 6 was performed within the EasySpin simulation package<sup>20</sup>. The hyperfine interaction  $A'$  with nuclear spins was not clearly resolved for all  $g$ -factor components, but its effect is clear for the lowest  $g$ -factors (or the highest resonance field part of the spectra). To fully describe the experimental spectra, hyperfine interaction  $A'$  and an anisotropic convolutional broadening  $\Delta B$  (full-width at half-height) were included in the simulation. The obtained parameter set is summarised in Table 1. Possible disorder in **1** yielding two different sets of the parameters was not distinguished in the experimental EPR spectra, possibly due to their small variation. When applying the Griffith-Figgis formalism<sup>21</sup> to obtain the effective  $g$ -factors of the ground Kramers doublet, it seems that both positive and negative axial field parameters  $|\Delta_{\text{ax}}| \approx 1050 \text{ cm}^{-1}$  seem to be in line with expected values if a substantial rhombic  $\Delta_{\text{rh}} / \Delta_{\text{ax}} \approx 1/3$  parameter is included for **1**. This confirms the critical role of the rhombic term in the description of magnetic properties of **1**. In the case of **2**, the only compatible combination of  $\Delta_{\text{rh}}$  and  $\Delta_{\text{ax}}$  seems to be when  $\Delta_{\text{ax}} \approx 1050 \text{ cm}^{-1}$  and the ratio of  $\Delta_{\text{rh}} / \Delta_{\text{ax}} \approx 0.104$ . The prediction of the effective  $g$ -factors for both complexes is shown in Figures S10 and S11. The results are consistent with the predicted positive  $D$  parameter from SA-CASSCF/NEVPT2 calculations for **2**. On the other hand, only judging from EPR analysis, the sign of  $D$  for **1** cannot be unambiguously identified. But taking into account the results of the magnetic data analysis and CAS(11e, 12o) SA-CASSCF/NEVPT2 calculations, both complexes can be considered with  $D > 0$ . In such case, one can assign  $g'_x, g'_y, g'_z$  and later to real  $g_x, g_y, g_z$  of spin Hamiltonian formalism using an approach outlined in ref.<sup>22</sup> Using all possible combinations of  $g'_1, g'_2, g'_3$  and the average  $g$ -factor obtained from the experimental room-temperature value of the effective magnetic moment one obtains the  $E/D$  ratio and a unique assignment of  $x, y, z$ -components of the  $g$ -factors and anisotropic hyperfine interaction  $A$ . Unfortunately, the values of  $D$  and  $E$  directly cannot be estimated from such analysis of X-band EPR spectra. The results of this procedure summarised also in Table 1 are in good agreement with the analysis of the magnetic data. The obtained  $E/D$  values of 0.235 and 0.078 for **1** and **2**, respectively, seem to be slightly underestimated. This is potentially affected by the accuracy in the estimation of the diamagnetic and temperature-independent paramagnetic contribution of the system to obtain the average  $g$ -factor from the room-temperature value of the magnetic moment required for the analysis.



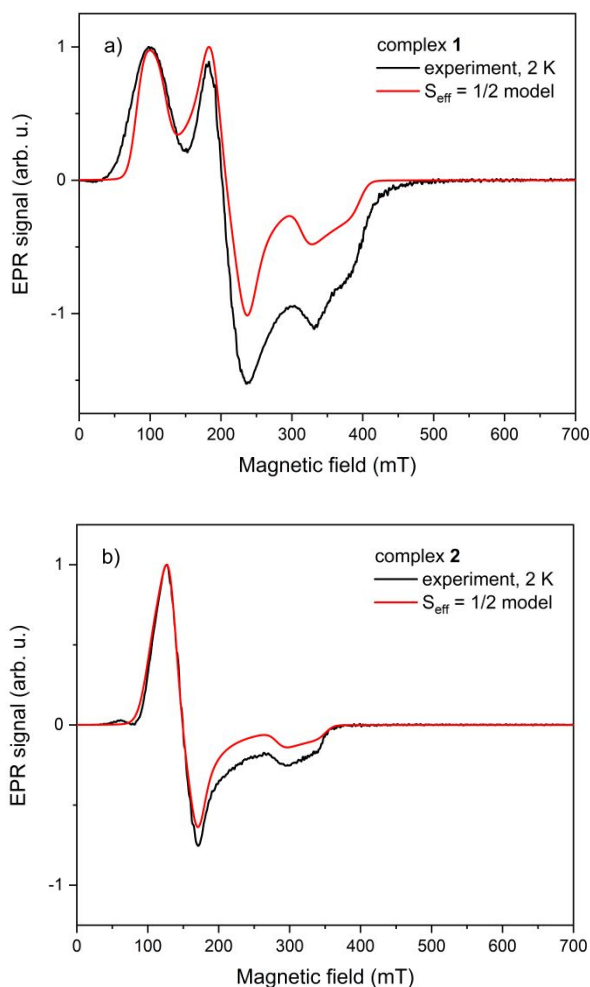


Figure 6 – The X-band EPR data (black solid lines) of complex **1** (a) and **2** (b) obtained at 2 K, including the simulations using the effective spin  $S_{\text{eff}} = 1/2$  model (solid red lines) with parameters summarised in Table 1.

Table 1 – Parameters of the effective spin  $S_{\text{eff}} = 1/2$  model and spin Hamiltonian formalism estimated for the analysis of the X-band EPR for complexes **1** and **2**.

Complex, approach	Parameters
1, $S_{\text{eff}} = 1/2$ model, estimated from data	$[g'_1, g'_2, g'_3] = [1.89, 3.17, 6.57]$ $[A'_1, A'_2, A'_3] = [275, 275, 470]$ MHz $[\Delta B_1, \Delta B_2, \Delta B_3] = [22, 38, 75]$ mT
1, $S_{\text{eff}} = 1/2$ model, $x, y, z$ assignment	$[g_x, g_y, g_z] = [3.17, 6.57, 1.89]$ $[A_x, A_y, A_z] = [275, 470, 275]$ MHz
1, spin Hamiltonian, $x, y, z$ assignment	$[g_x, g_y, g_z] = [2.49, 2.55, 2.22]$ $[A_x, A_y, A_z] = [216, 182, 323]$ MHz $E/D = 0.235$
2, $S_{\text{eff}} = 1/2$ model, estimated from data	$[g'_1, g'_2, g'_3] = [2.12, 4.47, 5.55]$ $[A'_1, A'_2, A'_3] = [255, 310, 400]$ MHz $[\Delta B_1, \Delta B_2, \Delta B_3] = [22, 38, 75]$ mT
2, $S_{\text{eff}} = 1/2$ model, $x, y, z$ assignment	$[g_x, g_y, g_z] = [4.47, 5.55, 2.12]$ $[A_x, A_y, A_z] = [310, 400, 255]$ MHz
2, spin Hamiltonian, $x, y, z$ assignment	$[g_x, g_y, g_z] = [2.54, 2.50, 2.16]$ $[A_x, A_y, A_z] = [176, 180, 260]$ MHz $E/D = 0.078$

Theoretical calculations

View Article Online  
DOI: 10.1039/D5DT01004G

Geometry optimizations and ZFS parameters were obtained by ORCA 5.0.4 software.<sup>23,24</sup> Complex cations were extracted from crystal structures and positions of hydrogens were first optimized by DFT method utilizing BP86 functional.<sup>25</sup> Ahlrichs' def2-TZVP basis set was chosen for all atoms except for hydrogen and carbon, where a less demanding def2-SVP basis set was chosen.<sup>26</sup> The resolution of identity (RI) approximation<sup>27</sup> together with def2/J auxiliary basis set<sup>28</sup> was employed. To obtain ZFS parameters, post-Hartree-Fock method CASSCF(7e, 5o)<sup>29</sup> with NEVPT2 correction<sup>30,31</sup> was used. The same basis sets were used with the addition of def2-TZVP/C for correlation fitting<sup>32</sup> and chain-of-sphere approximation<sup>33</sup> (RIJCOSX) was turned on. Obtained ZFS parameters are summarized in Table 2 for the active space defined by five metal 3d-orbitals, CAS(7e, 5o), and also for larger active space defined by two additional ligand base bonding orbitals and extra five 4d-orbitals, CAS(11e, 12o) – Figure S12.

Table 2 – Comparison of zero-field splitting parameters obtained from theoretical calculations and experimental data analysis.

Compound	1	2
Fitted parameters from experimental DC data		
$D$ (cm <sup>-1</sup> )	49.9	59.5
$E/D$	0.307	0.147
$g_{xy}$	2.470	2.347
$g_z$ (fixed)	2.0	2.0
CASSCF/NEVPT2 results with CAS(7e, 5o)		
$D$ (cm <sup>-1</sup> )	54.1/-57.0	53.7
$E/D$	0.328/0.330	0.121
$g_x$	2.353/2.342	2.458
$g_y$	2.752/2.020	2.625
$g_z$	2.031/2.777	2.035
$g_{\text{iso}}$	2.379/2.380	2.372
Kramers doublet with the effective spin of $S_{\text{eff}} = 1/2$		
$g_1$	1.593/1.572	2.057
$g_2$	2.381/2.327	3.983
$g_3$	7.428/7.513	6.052
$g_{\text{avg}}$	3.800/3.804	4.031
CASSCF/NEVPT2 results with CAS(11e, 12o)		
$D$ (cm <sup>-1</sup> )	52.6/55.4	53.0
$E/D$	0.326/0.331	0.116
$g_x$	2.354/2.343	2.461
$g_y$	2.753/2.777	2.629
$g_z$	2.027/2.016	2.031
$g_{\text{iso}}$	2.378/2.379	2.374
Kramers doublet with the effective spin of $S_{\text{eff}} = 1/2$		
$g_1$	1.606/1.595	2.073
$g_2$	2.396/2.363	4.031
$g_3$	7.416/7.486	6.018
$g_{\text{avg}}$	3.806/3.815	4.041

Due to the presence of disorder, both complex species of **1** were analyzed separately (labeled as **1\_a** and **1\_b**). The calculated splitting of d-orbitals for **1** and **2** resembles the pattern typical for pseudo-octahedral coordination geometry, set of  $t_{2g}$  and  $e_g$  orbitals, and  $e_2$  orbitals are more split for **1** than for **2** (Figure 7a). Due to lower symmetry,  ${}^4T_{1g}$  ligand-field term (in ideal  $O_h$  symmetry) is split into three terms within ca 1600



$\text{cm}^{-1}$  (Figure 7b). Finally, spin states for  $S = 3/2$  are split into two Kramers states separated by ca 120-128  $\text{cm}^{-1}$  for **1** and by 108  $\text{cm}^{-1}$  for **2**. Other excited Kramers states are located at much higher energies, thus, the spin Hamiltonian formalism is valid. Both complexes possess large magnetic anisotropy and non-zero rhombicity. This is in good agreement with the fitted values from DC magnetic measurements. Complexes may possess both easy-axis and easy-plane type of anisotropy due to high rhombicity,<sup>34</sup> we therefore analyzed ground state Kramers doublet ( $S_{\text{eff}} = 1/2$ ), which resulted in  $g_1, g_2 < g_{\text{avg}}$  and  $g_{\text{avg}} < g_3$  and we can thus conclude that both complexes possess the axial type of magnetic anisotropy. It is also demonstrated in Figure S13, in which respective D-tensors and three-dimensional magnetization data overlaid over respective molecular structures are depicted. Moreover, this finding is also in good agreement with AC magnetic measurements, as the axial type of magnetic anisotropy is needed for the observed slow relaxation of magnetization. Additional analysis with the SINGLE\_ANISO module also showed a large predisposition to quantum tunnelling between ground states with opposite magnetization with matrix elements of the transversal magnetic moment being equal to 0.666/0.659 and 1.02 for complexes **1** and **2**, respectively (Figure S13). We presume that this is the major contributing factor to why no slow relaxation was observed in the zero DC field.

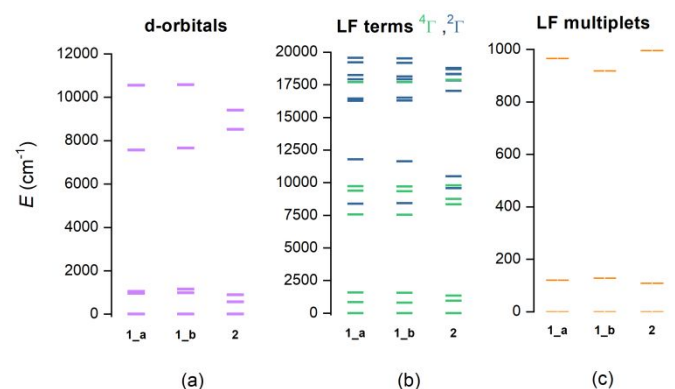


Figure 7 – Results of the CASSCF/NEVPT2 calculations for **1** and **2**: a) the plot of the d orbital splitting calculated by ab initio ligand field theory (AILFT) using CAS(7e, 5o), b) low-lying ligand-field terms (LFT) and c) ligand-field multiplets (LFM) resulted from CAS(11e, 12o). Note: different multiplicities of LFT are shown in different colors.

### Irradiation studies

In order to determine if our complexes undergo photoisomerisation, we investigated the effect of UV irradiation utilizing UV/Vis spectroscopy. Methanol solutions of complexes (10  $\mu\text{M}$ ) were subjected to 254 nm UV lamp (9 W) for 10-minute intervals between measurements.

For complex **1** (Figure 8 – top), we can see a gradual decrease in absorbance, as should be expected in the case of the formation of *cis* isomer, however, more irradiation causes continual drop below the absorbance level of pure *cis*-isomeric complex **2**. We therefore suspect that isomerization is accompanied by other side-reactions, most likely [2+2] cycloaddition.

This was confirmed when we performed the same experiment for complex **2** (Figure 8 – bottom) where a first increase of absorbance could be observed due to the formation of *trans* isomer. When equilibrium was reached, more irradiation only led to unwanted side reactions as is evident from the continual drop of absorbance even below the level before irradiation. Interestingly, the band around 200 nm increases with prolonged irradiation in contrast to complex **1**. It is possible that different side products are created for both complexes.

A sudden drop or rise of 270 nm band can be observed for **1** and **2**, respectively, while 230 nm band absorbance drops only slightly for both compounds after the first 10 minutes of irradiation. Any further irradiation leads to a slow decrease of both bands, which supports our hypothesis that photoequilibrium of both isomers is achieved within the first 10 minutes of irradiation, and further irradiation leads to degradation. Unfortunately, the isomers cannot be selectively switched by different wavelengths as their absorbance maxima are nearly identical and differ only in extinction coefficients.

The same experiment was performed for deprotonated forms of both isomers of cinnamic acid, where a similar trend was observed (Figure S14). We, therefore, conclude that our complexes undergo photoisomerization, which is, however, accompanied by side reactions that lead to the degradation of the complexes.

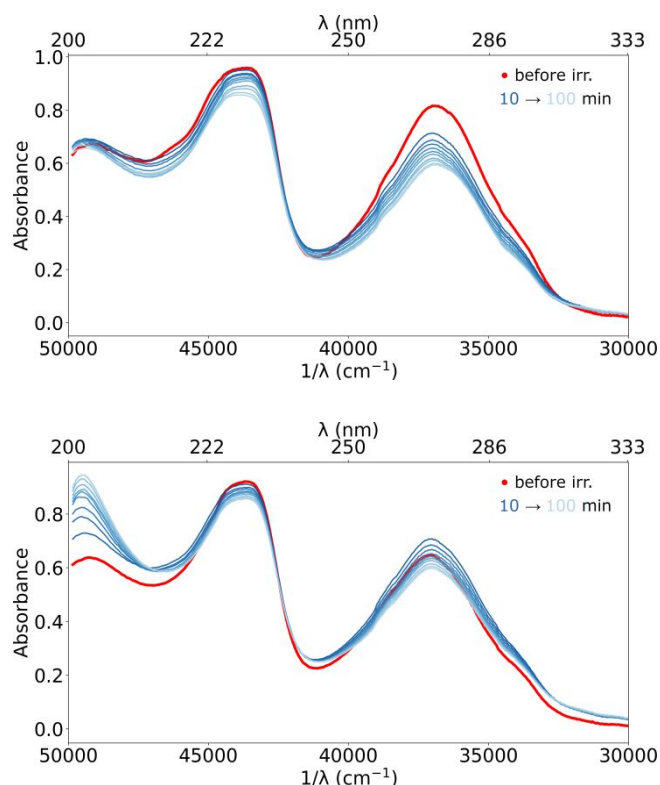


Figure 8 – UV/Vis spectrum of complex **1** (top) and **2** (bottom) before and after irradiation with 254 nm lamp.

Additionally, DFT/TD-DFT calculations were done with ORCA 6.0<sup>35</sup> in order to calculate UV-VIS spectra of both *trans/cis* isomers of cinnamate, their complexes **1** and **2**, and also



possible products of photodimerization of *trans*-cinnamate, namely, dianions of  $\alpha$ -truxillic acid and  $\beta$ -truxinic acid. First, the molecular geometries were optimized with range hybrid CAM-B3LYP functional<sup>36</sup> with D4 dispersion correction<sup>37</sup> using C-PCM solvation model for methanol.<sup>38,39</sup> Next, TD-DFT calculations were performed with the same functional, and respective UV-VIS spectra are shown in Figure 9. The calculated dominant bands of cinnamates located within 38-40 000  $\text{cm}^{-1}$  are shifted to higher energies for *cis*-cinnamate (band maximum located at 39 757  $\text{cm}^{-1}$ ) in comparison with *trans*-cinnamate (band maximum located at 38 423  $\text{cm}^{-1}$ ). With the help of Natural Transition Orbitals (NTOs), these transitions were assigned to  $\pi \rightarrow \pi^*$  transitions involving the double bond of cinnamate (Figures S15 and S16). The TD-DFT results of Co(II) complexes **1** and **2** showed that band maxima are located at 39049  $\text{cm}^{-1}$  for **1** and at 39709  $\text{cm}^{-1}$  for **2** (Figure 9). These bands have two main contributions as deduced from respective NTOs, the first one located at lower energies comes from  $\pi \rightarrow \pi^*$  transitions of cinnamate ligand, and the second one comes from  $\pi \rightarrow \pi^*$  and LMCT transitions of neocuproine ligands (Figures S17 and S18). This is in accordance with the spectrum calculated for free neocuproine (Figure 9). It is worth mentioning that dianions of  $\alpha$ -truxillic acid and  $\beta$ -truxinic acid, possible outcomes of photoreactions, should absorb the light at much higher energy.

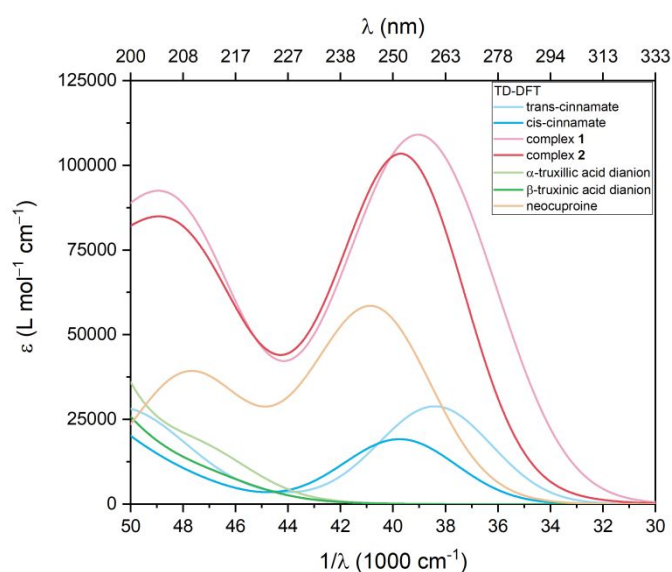


Figure 9 – UV-VIS spectra calculated by TD-DFT on optimized molecular geometries using PBE0 hybrid functional.

Moreover, the theoretical evolution of the UV-VIS spectra following the *trans*↔*cis* isomerization of the cinnamate anion and Co(II) complex  $[\text{Co}(\text{neo})_2(\text{cin})]^+$  were calculated as depicted in Figure 10. It suggests that the main band at 38-40 000  $\text{cm}^{-1}$  should lose the intensity and shift to higher energies during *trans*→*cis* reaction and these changes are much more pronounced in free cinnamate anion than in the respective Co(II) complex. This agrees with experimental observation for **1** (Figure 8, top) and *trans*-cinnamate (Figure 8, top), and for short-term (ca up to 10 minutes) photoirradiation experiments for **2** (Figure 8, bottom) and *cis*-cinnamate (Figure 8, bottom).

This suggests that the production of photodegradation side products is enhanced in **2**.

DOI: 10.1039/D5DT01004G

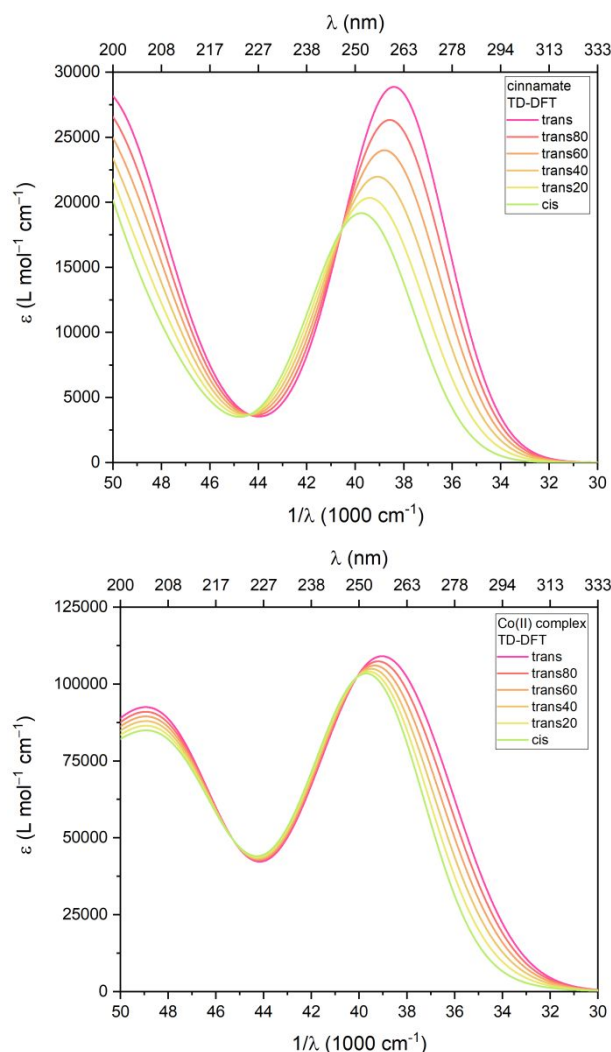


Figure 10 – UV-VIS spectra calculated by TD-DFT on optimized molecular geometries using PBE0 hybrid functional showing *trans*-*cis* isomerization for cinnamate anion (top) and for Co(II) complex (bottom).

## Experimental

### Preparation of n-butylammonium *cis*-cinnamate

1 mmol of *trans*-cinnamic acid was dissolved in 100 ml of acetonitrile in a 250 ml quartz Erlenmeyer flask. To this 1.1 mmol of n-butylamine was added and the mixture was subjected to UV irradiation with a medium-pressure mercury lamp for 4 hours under constant stirring (**CAUTION:** care must be taken to protect eyes and skin from intense UV radiation, protective gear and glasses should be used during irradiation, working in a fume hood is advisable as the lamp produces ozone). The mixture was then cooled in a fridge to complete the crystallization. The solid product was filtered off under reduced pressure and dried on air. Yield: 106 mg (48 %). Purity was confirmed by <sup>1</sup>H NMR, which was in accordance with the published spectrum<sup>16</sup> with coupling constant <sup>3</sup>J<sub>HH</sub> between C=C



hydrogens of 12.7 Hz, typical for *cis* isomer of cinnamic acid (Figure S1).

#### Synthesis of complex 1

36.6 mg (0.1 mmol) of  $\text{Co}(\text{ClO}_4)_2 \cdot 6\text{H}_2\text{O}$  was dissolved in 5 ml of acetone together with 43.4 mg (0.2 mmol) of neocuproine hemihydrate. To this was added a solution of 14.8 mg (0.1 mmol) of *trans*-cinnamic acid with 13.8  $\mu\text{l}$  (0.1 mmol) of triethylamine in 5 ml of acetone under stirring. Pink solid product was obtained by reducing the volume to 3 ml by blowing nitrogen gas and stirring overnight. Red crystals were filtered off, washed with a small amount of cold acetone, and dried in air. Red block single crystals of X-ray diffraction quality were obtained by undisturbed slow evaporation of the solvent. Yield: 44 mg (61 %). FT-IR ( $\text{cm}^{-1}$ ): 3062(w), 3021(w), 1708(w), 1631(w), 1590(m), 1564(w), 1541(w), 1496(s), 1451(m), 1421(m), 1359(m), 1294(w), 1246(w), 1224(w), 1153(w), 1073(vs), 979(m), 860(s), 815(w), 778(m), 731(m), 718(w), 693(w), 681(w), 655(w), 621(m), 584(w), 551(w), 435(w). Anal. calcd for  $\text{C}_{37}\text{H}_{33}\text{ClCoN}_4\text{O}_6$ : C, 61.6; H, 4.3; N, 7.8. Found: C, 60.9; H, 4.3; N, 7.8.

#### Synthesis of complex 2

36.6 mg (0.1 mmol) of  $\text{Co}(\text{ClO}_4)_2 \cdot 6\text{H}_2\text{O}$  was dissolved in 5 ml of acetone together with 43.4 mg (0.2 mmol) of neocuproine hemihydrate. To this was added a solution of 22.1 mg (0.1 mmol) of *n*-butylammonium *cis*-cinnamate in 5 ml of acetone with a few drops of water to dissolve the salt under stirring. Complex **2** precipitated within minutes after the addition of the *cis*-cinnamate salt and was left stirring overnight. Pink microcrystals were filtered off, washed with acetone, and dried in air. Pink single crystals suitable for X-ray diffraction analysis were prepared by using 0.1 molar equivalents of reactants with the same volume of solvent and leaving the solution undisturbed in a fridge overnight. Yield: 63 mg (87 %). FT-IR ( $\text{cm}^{-1}$ ): 3066(w), 3019(w), 1705(w), 1626(w), 1591(m), 1563(w), 1533(m), 1496(s), 1465(m), 1436(s), 1361(s), 1327(w), 1294(w), 1224(w), 1153(w), 1084(vs), 1034(m), 859(s), 848(m), 810(w), 772(w), 731(w), 701(w), 655(w), 621(m), 550(w). Anal. calcd for  $\text{C}_{37}\text{H}_{31}\text{ClCoN}_4\text{O}_6$ : C, 61.6; H, 4.3; N, 7.8. Found: C, 61.2; H, 4.3; N, 7.7.

#### Instrumentation

Elemental analysis (C,H,N) was performed on Thermo Scientific Flash 2000 analyzer. Infrared spectra were recorded on JASCO FT/IR-4700 spectrometer utilizing ATR technique. UV-VIS spectra were recorded on GBC Scientific Instruments Cintra 3030. X-ray powder diffraction was recorded on Rigaku MiniFlex 600. NMR spectra were measured on Varian 400 MHz NMR spectrometer. DC magnetic measurements were done on Quantum Design MPMS3. AC magnetic measurements were done on Quantum Design MPMS-XL. EPR spectra were measured on Bruker ELEXSYS II E500.

#### Crystallography

The X-ray diffraction data for orange crystals of **1** and **2** were collected using an XtaLAB Synergy-I diffractometer equipped with a HyPix3000 hybrid pixel array detector and a

microfocused PhotonJet-I X-ray source ( $\text{Cu K}\alpha$ , 1.54184 Å). Absorption corrections were applied using the program CrysAlisPro 1.171.40.82a.<sup>40</sup> The crystal structures were solved using SHELXT program<sup>41</sup> and refined using the full matrix least-squares procedure with SHELXL<sup>42</sup> in OLEX2 (version 1.5).<sup>43</sup> All non-hydrogen atoms were refined anisotropically, while hydrogen atoms were located from the Fourier difference map and refined using the “riding” model with  $U_{\text{iso}}(\text{H}) = 1.2(-\text{CH}_2)$  or  $1.5(-\text{CH}_3)U_{\text{eq}}$ . Powder diffraction data were collected using a MiniFlex600 (Rigaku) equipped with the Bragg–Brentano geometry, and with iron-filtered  $\text{CuK}\alpha_{1,2}$  radiation.

Non-routine aspects of refinement: In **1**, the cinnamate ligand is disordered over two positions, with the ratio of site occupation factors being 0.634:0.322. To build the model of disorder, it was necessary to use an extensive set of SHELXL restraints (SIMU, SADI) and constraints (EADP).

## Conclusions

The incorporation of *trans/cis*-isomers of cinnamic acid resulted in two Co(II) complexes, **1** and **2**, in which the carboxylic moiety is coordinated in a bidentate fashion. However, the respective Co–O bond distances are very uneven in **1** in contrast to **2**, resulting in the shape closer to the ideal octahedron for **2**. These distinctions in the ligand fields are reflected in different sizes of ZFS parameters, *D* and *E*, deduced from the analysis of DC magnetic data. The easy-axis type of magnetic anisotropy for both complexes was further confirmed experimentally with X-band EPR and theoretically with CASSCF/NEVPT2 calculations. Albeit both complexes underwent photoisomerization in the solution, longer exposure to the light resulted in side-reactions and degradations. To conclude, herein we provided evidence that different geometric isomers of the ligand alter both static and dynamic magnetic properties of these field-induced photoswitchable SMMs, however, their low photostability urges for other suitable molecular systems.

## Author contributions

Petr Halaš: formal analysis, investigation, software, visualization, writing – original draft. Ivan Nemeč: formal analysis, investigation. Erik Čizmar: formal analysis, investigation, visualization. Radovan Herchel: conceptualization, formal analysis, software, visualization, writing – review & editing.

## Conflicts of interest

There are no conflicts to declare.

## Data availability

The data supporting this article have been included as part of the Supplementary Information. Crystallographic data for compounds **1** and **2** have been deposited at the CCDC under



deposition numbers 2447436 and 2447437 and can be obtained from <https://www.ccdc.cam.ac.uk/structures/>.

## Acknowledgments

This research was funded by Palacký University in Olomouc projects IGA\_PrF\_2024\_009 and IGA\_PrF\_2023\_007. This work was also supported by the Slovak Research and Development Agency under Contracts APVV-20-0512, APVV-22-0172, and APVV-23-0006.

## Notes and references

- 1 F. S. Guo, B. M. Day, Y. C. Chen, M. L. Tong, A. Mansikkamäki and R. A. Layfield, *Science*, 2018, **362**(6421), 1400-1403.
- 2 B. Yao, M. K. Singh, Y. F. Deng, Y. N. Wang, K. R. Dunbar and Y. Z. Zhang, *Inorganic Chemistry*, 2020, **59**(12), 8505-8513.
- 3 S. Sottini, G. Poneti, S. Ciattini, N. Levesanos, E. Ferentinos, J. Krzystek, L. Sorace and P. Kyritsis, *Inorganic Chemistry*, 2016, **55**(19), 9537-9548.
- 4 Y. Rechkemmer, F.D. Breitgoff, M. Van Der Meer, M. Atanasov, M. Hakl, M. Orlita, P. Neugebauer, F. Neese, B. Sarkar and J. Van Slageren, *Nature communications*, 2016, **7**(1), 10467.
- 5 R. Herchel, L. Váhovská, I. Potočňák and Z. Travnicek, *Inorganic chemistry*, 2014, **53**(12), 5896-5898.
- 6 J. Vallejo, M. Viciano-Chumillas, F. Lloret, M. Julve, I. Castro, J. Krzystek, M. Ozerov, D. Armentano, G. De Munno and J. Cano, *Inorganic Chemistry*, 2019, **58**(23), 15726-15740.
- 7 S. Kume, M. Kurihara and H. Nishihara, *Chemical Communications*, 2001, (17), 1656-1657.
- 8 L. Chen, Y. Tan, H. Xu, K. Wang, Z.H. Chen, N. Zheng, Y.Q. Li and L.R. Lin, *Dalton Transactions*, 2020, **49**(46), 16745-16761.
- 9 V. Guerschais and H. Le Bozec, *Molecular organometallic materials for optics*, 2010, 171-225.
- 10 K. Rogacz, M. Brzozowska, S. Baś, K. Kurpiewska and D. Pinkowicz, *Inorganic Chemistry*, 2022, **61**(41), 16295-16306.
- 11 K. Rogacz, M. Magott, S. Baś, M. Foltyn, M. Rams and D. Pinkowicz, *RSC advances*, 2024, **14**(21), 14515-14522.
- 12 L. R. Lin, X. Wang, G. N. Wei, H. H. Tang, H. Zhang and L. H. Ma, *Dalton Transactions*, 2016, **45**(38), 14954-14964.
- 13 L. Chen, Y. Tan, H. Xu, K. Wang, Z.H. Chen, N. Zheng, Y.Q. Li and L.R. Lin, *Dalton Transactions*, 2020, **49**(46), 16745-16761.
- 14 P. Halaš, I. Nemeč and R. Herchel, *Magnetochemistry*, 2023, **9**(11), 229.
- 15 M. B. Hocking, *Canadian Journal of Chemistry*, 1969, **47**(24), 4567-4576.
- 16 M. L. Salum, C. J. Robles and R. Erra-Balsells, *Organic Letters*, 2010, **12**(21), 4808-4811.
- 17 R. Boča, R. Herchel, Program POLYMAGNET 2006–2021.
- 18 P. Virtanen, R. Gommers, T.E. Oliphant, M. Haberland, T. Reddy, D. Cournapeau, E. Burovski, P. Peterson, W.

- Weckesser, J. Bright and S.J. Van Der Walt, *Nature methods*, 2020, **17**(3), 261-272.
- 19 C. Rajnák and R. Boča, *Coordination Chemistry Reviews*, 2021, **436**, 213808.
  - 20 S. Stoll and A. Schweiger, *J. Magn. Reson.*, 2006, **178**, 42-55.
  - 21 A.V. Pali, D.V. Korchagin, E.A. Yureva, A.V. Akimov, E.Y. Misochko, G.V. Shilov, A.D. Talantsev, R.B. Morgunov, S.M. Aldoshin and B.S. Tsukerblat, *Inorg. Chem.*, 2016, **55**, 9696–9706.
  - 22 S. Gómez-Coca, A. Urtizberea, E. Cremades, P.J. Alonso, A. Camón, E. Ruiz and F. Luis, *Nat. Commun.*, 2014, **5**, 4300.
  - 23 F. Neese, F. Wennmohs, U. Becker and C. Riplinger, *The Journal of chemical physics*, 2020, **152**(22).
  - 24 F. Neese, *Wiley Interdisciplinary Reviews: Computational Molecular Science*, 2022, **12**(5), e1606.
  - 25 A. D. Becke, *Physical review A*, 1988, **38**(6), 3098.
  - 26 F. Weigend and R. Ahlrichs, *Physical Chemistry Chemical Physics*, 2005, **7**(18), 3297-3305.
  - 27 F. Neese, *Journal of computational chemistry*, 2003, **24**(14), 1740-1747.
  - 28 F. Weigend, *Physical chemistry chemical physics*, 2006, **8**(9), 1057-1065.
  - 29 P. Å. Malmqvist and B. O. Roos, *Chemical physics letters*, 1989, **155**(2), 189-194.
  - 30 C. Angeli, R. Cimiraaglia, S. Evangelisti, T. Leininger and J. P. Malrieu, *The Journal of Chemical Physics*, 2001, **114**(23), 10252-10264.
  - 31 C. Angeli, R. Cimiraaglia and J. P. Malrieu, *Chemical physics letters*, 2001, **350**(3-4), 297-305.
  - 32 A. Hellweg, C. Hättig, S. Höfener and W. Klopper, *Theoretical Chemistry Accounts*, 2007, **117**(4), 587-597.
  - 33 F. Neese, F. Wennmohs, A. Hansen and U. Becker, *Chemical Physics*, 2009, **356**(1-3), 98-109.
  - 34 I. Nemeč, R. Herchel, M. Kern, P. Neugebauer, J. Van Slageren and Z. Trávníček, *Materials*, 2017, **10**(3), 249.
  - 35 F. Neese, *WIREs Comput. Mol. Sci.*, 2025, **15**, e70019.
  - 36 T. Yanai, D. P. Tew and N. C. Handy, *Chem. Phys. Lett.*, 2004, **393**, 51–57.
  - 37 E. Caldeweyher, S. Ehlert, A. Hansen, H. Neugebauer, S. Spicher, C. Bannwarth and S. Grimme, *J. Chem. Phys.*, 2019, **150**, 154122.
  - 38 M. Garcia-Ratés and F. Neese, *J. Comput. Chem.*, 2020, **41**, 922.
  - 39 V. Barone and M. Cossi, *J. Phys. Chem. A*, 1998, **102**, 1995.
  - 40 Rigaku Oxford Diffraction (2020) CrysAlisPro 1.171.40.82a.
  - 41 G. M. Sheldrick, *Acta Crystallogr. Sect. A*, 2015, **71**, 3–8.
  - 42 L. J. Bourhis, O. V. Dolomanov, R. J. Gildea, J. A. K. Howard and H. Puschmann, *Acta Crystallogr. Sect. A*, 2015, **71**, 59–75, doi:10.1107/S2053273314022207.
  - 43 O. V. Dolomanov, L. J. Bourhis, R. J. Gildea, J. A. K. Howard and H. Puschmann, *J. Appl. Crystallogr.*, 2009, **42**, 339–341.



## Data availability

The data supporting this article have been included as part of the Supplementary Information. Crystallographic data for compounds 1 and 2 have been deposited at the CCDC under deposition numbers 2447436 and 2447437 and can be obtained from <https://www.ccdc.cam.ac.uk/structures/>.

